



This article appeared in a journal published by Elsevier. The attached copy is furnished to the author for internal non-commercial research and education use, including for instruction at the authors institution and sharing with colleagues.

Other uses, including reproduction and distribution, or selling or licensing copies, or posting to personal, institutional or third party websites are prohibited.

In most cases authors are permitted to post their version of the article (e.g. in Word or Tex form) to their personal website or institutional repository. Authors requiring further information regarding Elsevier's archiving and manuscript policies are encouraged to visit:

<http://www.elsevier.com/copyright>



Contents lists available at SciVerse ScienceDirect

## International Journal of Adhesion &amp; Adhesives

journal homepage: [www.elsevier.com/locate/ijadhadh](http://www.elsevier.com/locate/ijadhadh)

## Adhesive joints in composite laminates—A combined numerical/experimental estimate of critical energy release rates

C. Balzani<sup>a,\*</sup>, W. Wagner<sup>a</sup>, D. Wilckens<sup>b</sup>, R. Degenhardt<sup>b</sup>, S. Büsing<sup>c</sup>, H.-G. Reimerdes<sup>c</sup><sup>a</sup> Karlsruhe Institute of Technology (KIT), Institute for Structural Analysis, Kaiserstr. 12, D-76131 Karlsruhe, Germany<sup>b</sup> German Aerospace Center (DLR), Institute of Composite Structures and Adaptive Systems, Lilienthalplatz 7, D-38108 Braunschweig, Germany<sup>c</sup> RWTH Aachen University, Department of Aerospace and Lightweight Structures, Willnerstr. 7, D-52062 Aachen, Germany

## ARTICLE INFO

## Article history:

Accepted 20 August 2011

Available online 16 September 2011

## Keywords:

Adhesive joint

Cohesive interface element

Composite laminate

Material characterization

Critical energy release rate

Fracture toughness

## ABSTRACT

The characterization of critical energy release rates of adhesive joints in laminated composite structures is a key issue when failure analyses have to be performed. Critical energy release rates, or fracture toughnesses, are known to be dependent on the mode mixing ratio, i.e. the portion of shear loading. It is thus useful to determine a criterion which gives the critical energy release rate as a function of the mode mixing ratio, which is the overall goal of this paper. For this purpose several experiments have been performed, for single mode I, single mode II, and mixed mode I/II loading conditions with pre-defined mode mixing ratios. Unfortunately, most of the experimental outcome cannot be used directly for least squares fitting of suitable fracture toughness criteria due to a couple of reasons, which will be discussed in detail. Hence, a numerical approach based on cohesive interface elements is employed to determine some of the critical energy release rates by fitting against experimental load–deformation curves. This combined numerical/experimental approach yields a useful database of discrete critical energy release rate values. These are utilized to fit suitable criteria which then allow the calculation of critical energy release rates for any given mode mixing ratio. The results are discussed in terms of convergence to the discrete values and physical plausibility, and a simple possibility to include mode III behavior is presented.

© 2011 Elsevier Ltd. All rights reserved.

## 1. Introduction

Adhesive bonding as a technology for joining two composite parts together becomes more and more popular in manufacturing large-scale composite structures. Besides the ease of disassembly, the drawbacks of mechanical fasteners are that rivets or bolts can cause significant weight and aero/aquodynamic penalties, and that they act as stress concentrators which may produce local damage. Further, the cut-out or drilling of holes is often related with severe splintering or delamination. Adhesive bonding technology produces plane surfaces without holes which significantly reduces such problems. Compared with co-curing technology secondary adhesive bonding has several advantages: first, the designer has more flexibility in shape. For instance, the pitch between stiffeners in stiffened structures can easily be varied. Second, the tooling process is much easier. Third, also the lay-up process is less complicated, especially if complex geometries can be substructured into several simple geometries. Since the lay-up is often the most time-consuming manufacturing process [1], secondary adhesive bonding can save a lot of time in many cases.

In the design phase of composite structures failure analyses are often employed which require accurate and reliable characterization of the material properties. For adhesive bonds these are the strength parameters and the critical energy release rate (CERR) values characterizing the toughness of the material. The CERRs are the most governing parameters. They have a more severe impact on the load-carrying capacity than the strength parameters. Fig. 1 shows load–displacement curves of a double cantilever beam (DCB) test.<sup>1</sup> Therein, a numerical parameter study is performed where the strength is varied while keeping the fracture toughness constant, Fig. 1(a), and vice versa, Fig. 1(b). For the simulation the numerical model described in Section 3.1 was used, and the results are normalized by the maximum load and the corresponding cross-head displacement. As seen, the strength can be reduced significantly (factor of 10) without changing the maximum load too much. In contrast to that, a small change in CERR has a significant impact on the maximum load. Following from this, the characterization of CERRs is extraordinarily relevant for damage tolerance analyses.

The response within an adhesive layer is very similar to that in a co-cured interface. The stresses governing a debonding process

\* Corresponding author. Tel.: +49 721 608 46129; fax: +49 721 608 46015.  
E-mail address: [claudio.balzani@kit.edu](mailto:claudio.balzani@kit.edu) (C. Balzani).

<sup>1</sup> For details about the DCB test see Section 2.1.

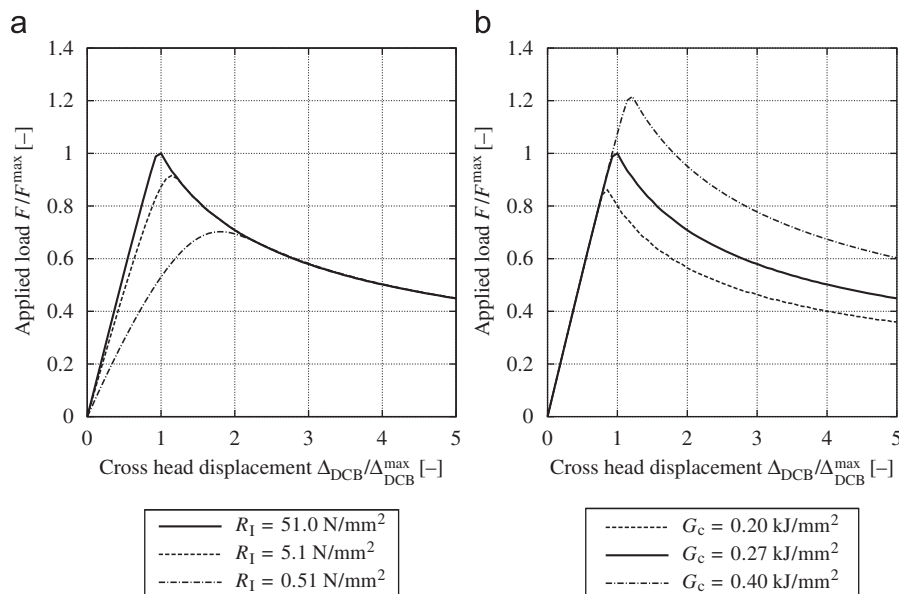


Fig. 1. Parameter study on a DCB test: variation of the mode I strength (a) and the mode I CERR (b).

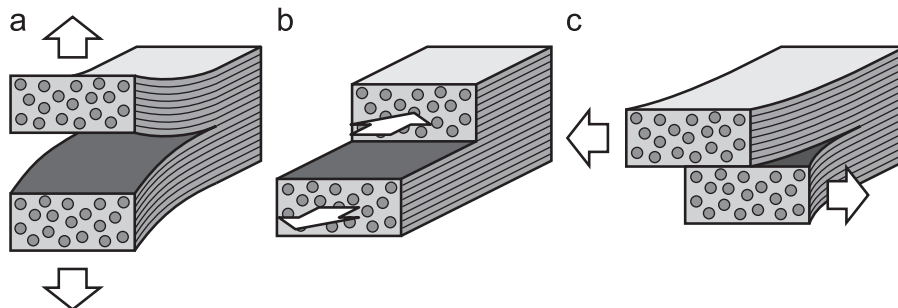


Fig. 2. Sketch of the three delamination mechanisms: mode I normal opening (a), mode II sliding shear (b), and mode III scissoring shear (c).

are the normal tensile stress perpendicular to the adhesive plane and the shear stresses parallel to the adhesive plane, which are also responsible for delamination. Hence, the debonding mechanisms of an adhesive joint can be classified in the well known delamination modes [2,3]: mode I normal opening, mode II sliding shear, and mode III scissoring shear. These failure modes are illustrated in Fig. 2.

In the general case an adhesive joint is of course exposed to a mixture of these modes. The specific mode mixture has a major impact on the adhesive CERR: the larger the shear portion the larger the CERR becomes [4,5], a phenomenon well known from studies of interlaminar CERRs [6,7]. It is very important to capture this effect in characterization schemes, which consequently have to include experimental techniques for several mode mixtures. It is common practice to utilize the same experiments standardized for the determination of the interlaminar fracture toughness, e.g. DCB tests [8–11] for single mode I, end notched flexure (ENF) tests [11,12] for single mode II, and mixed mode bending (MMB) tests [13–18] for mixed mode I/II loading conditions. It should be mentioned that from Ref. [10] a standard has been developed for the determination of the adhesive fracture toughness [19] as it has been previously recognized that bonded and co-cured systems offer many similarities.

A lot of research has been performed in the past dealing with adhesive CERRs. Especially the research groups around Blackman and Kinloch published a lot of fundamental work. In [20–22], the influence of the loading rate was investigated, a topic recently revisited in [23,24], where the fracture toughness turned out to

decrease significantly on increasing the loading rate. The influence of the kind of substrates on the adhesive glass transition temperature, and consequently on the mode I fracture toughness  $G_{Ic}$ , was reported in [25]. The test geometry (DCB or tapered DCB test) had no influence. It was also reported that adhesive pastes are very sensitive to the pre-bond moisture content of the substrates, while film adhesives are not [26]. An investigation of adhesive repair joints after pre-conditioning in a hot/wet environment was performed in [27] followed by finite element modeling [28]. It was figured out that the pre-conditioning had no significant effect on the static strength, though a change in failure modes was observed, but the fatigue strength decreased significantly. Very recently – and very important in the context of this paper – Dillard et al. [29] reported that the adhesive fracture toughness under mixed mode loadings may be lower than the single mode ones. This clearly stands in contrast to [4,5]. Actually, this effect was caused by the failure mechanism changing from a cohesive one in the adhesive to an adhesive one in the carrier cloth/adhesive interface. Since the adhesive under investigation does not contain any carrier cloth, the appearance of such an effect is not expected here.

In this paper the following research activities are reported: several experiments have been carried out for characterizing the fracture toughness of a film adhesive in single mode I, single mode II, and mixed mode I/II loading conditions. The adhesive was used to connect unidirectional carbon/epoxy composite plates. The aim of the paper is to study the influence of the mode mixing ratio, i.e. the shear portion within the interface, on the

CERR, and to evaluate and validate criteria from the literature which give the mixed mode CERR as a function of the mode mixing ratio. Unfortunately, the mixed mode test results (and also those for single mode II) cannot directly be employed to fit the CERR criteria due to a couple of reasons, which are explained in detail at a later stage of this paper. A numerical model is utilized to fit the mixed mode fracture toughness values for the investigated mode mixing ratios against the experimental load–deformation curves. The obtained discrete values of the CERR are employed for fitting the CERR criteria. These serve to calculate the mixed mode CERR for any given mode mixing ratio. The results are discussed in terms of physical plausibility, convergence to the discrete CERR values, and finding the single mode II CERR from the CERR criteria. Finally, a simple method to include mode III behavior is presented, which is believed to be slightly different from that in mode II.

## 2. Experimental framework

The material under investigation is Cytec FM 300 M film adhesive [30] connecting Hexcel UD IM7/8552 carbon/epoxy laminates [31]. The adhesive is a high shear strength modified epoxy resin providing excellent bondline and flow control and reducing the tendency to trap air during lay-up. The composite is based on prepreg technology. It is a high-performance laminate which is commonly used in the aircraft industry for highly stressed primary structures.

The test specimens were manufactured by fabricating unidirectional composite plates (containing only  $0^\circ$  plies) which were subsequently bonded with the adhesive film (thickness  $t_{adh} = 0.13$  mm) while inserting a thin layer of polytetrafluoroethylene (PTFE) to generate a pre-crack. The bonded plates were then cut into the desired sizes for the different tests, which are described in Sections 2.1–2.3. The composite plates were cured in accordance with the product data sheet [31]. The adhesive film is treated as double-sided tape. Protection foils are removed prior to bonding. The adhesive was cured for 60 min at a pressure between 15 and 100 psi (in accordance with the product data sheet [30]).

The experiments performed in the context of this paper include DCB, ENF, and MMB tests. The European standards DIN-EN 6033 [9] and DIN-EN 6034 [12] were applied for the DCB and ENF tests, respectively. The American standard ASTM

D6671 [18] was employed for the MMB tests. It may be mentioned that the substrates remained elastic in all cases. To distinguish the different loading scenarios (single mode I, single mode II, or mixed mode I/II) we introduce a mode mixing ratio  $\beta$  which is defined by the expression

$$\beta := \frac{G_{II}}{G_I + G_{II}}, \quad (1)$$

where  $G_I$  and  $G_{II}$  are the mode I and mode II strain energy release rates. Hence, the larger the shear portion within the adhesive the larger the mode mixing ratio becomes. Single mode I is defined by a mode mixing ratio of  $\beta = 0$  while single mode II is defined by  $\beta = 1$ . Three different mode mixities (0.25, 0.5, and 0.75) are investigated in the MMB tests. The testing procedures and the specimen geometries are described in the sequel, and the experimental results are presented.

### 2.1. Single mode I

The subject of this section is the experimental determination of  $G_{Ic}$  via a DCB test. The test setup is illustrated in Fig. 3. The test series consists of 14 specimens. The composite plates from which the specimens are fabricated are laminated with a  $[0^\circ]_{16}$  sequence. The thickness of one layer is  $t_l = 0.125$  mm and that of a plate is  $t = 2.0$  mm. The PTFE insert has a thickness of  $t_{PTFE} = 0.02$  mm. The pre-crack length is denoted by  $a_0$  and the crack length after propagation by  $a$ . Both are measured from the load-line in the aluminum blocks introducing the load up to the crack front. To avoid any influence of the PTFE insert the specimens were additionally pre-cracked by 10–15 mm in single mode I. Note that the initial crack length  $a_0$  includes the additional pre-crack. The intact adhesive area has the length  $l_{adh}$ . The specimen width is denoted by  $w$ . Table 1 lists the average geometrical magnitudes. The applied load is denoted by  $F$ , the cross-head displacement by  $\Delta_{DCB}$ , and the maxima of the applied load and the cross-head

**Table 1**  
Geometrical data for the DCB and ENF test specimens (in mm).

Test type	$l_{adh}$	$a_0$	$w$	$t$
DCB	209.04	20.96	25.00	2.00
ENF	65.00	35.00	25.00	2.00

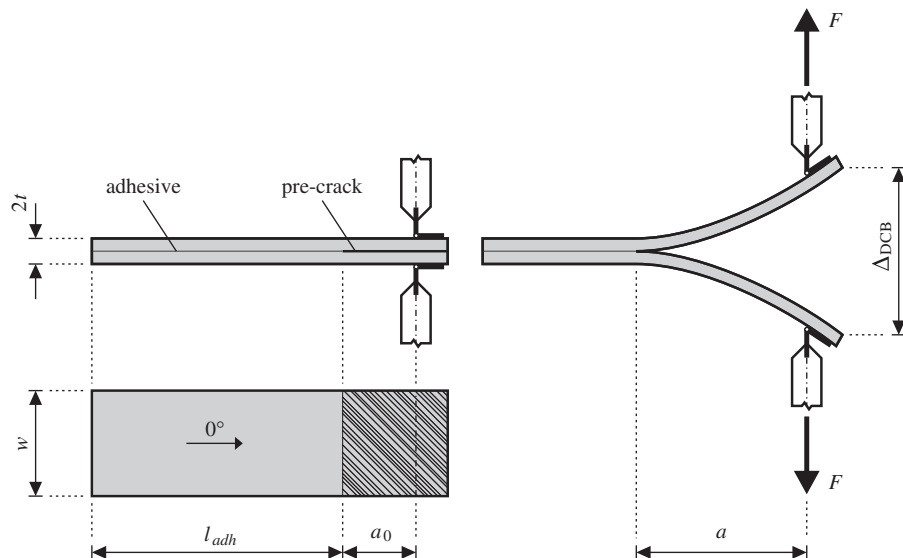


**Fig. 3.** Illustration of the DCB test setup and the specimen geometry (top left: initial configuration; bottom left: vertical projection of the test specimen; right: loaded configuration).

displacement by  $F^{\max}$  and  $\Delta_{\text{DCB}}^{\max}$ , respectively. The tests are performed under displacement-control with a quasi-static loading rate of 10 mm/min until the crack length reaches approximately  $a=100$  mm.

The data reduction scheme employed within the applied standard works as follows: Load–deformation curves are recorded during the entire duration of the tests. A sketch of a characteristic curve is depicted in Fig. 4(a). The curve is normalized by the maximum values of the load and the cross-head displacement, thus the maxima are equal to unity. The fracture toughness is the energy dissipated on crack propagation (dashed area in Fig. 4(a)) related to the size of the fracture surface. The amount of the dissipated energy can be calculated by determining the total energy and then subtracting the elastic energy stored in the laminate plates. The total energy is obtained by calculating the area under the loading path of the experimental curve. For this purpose the curve is subdivided into  $n-1$  intervals between the  $n$  data points. The size of the areas under the curve intervals is computed using the midpoint rule. Summarizing these areas yields the total energy introduced into the system. The elastic energy stored within the laminate plates is obtained with the same technique for the unloading path of the experimental curve. The crack lengths before and after the tests are marked on both sides of the specimens. The distance between these marks (average of the values on both sides of the specimens) times the width of the specimens is the size of the fracture surface. The data reduction scheme is based on direct energy measurements and not on calculations based on beam theory. It is thus not necessary to correct the data for beam root rotation, transverse shear, large displacements, or end block stiffening. It should be mentioned that in some cases stick-slip occurred, but no special actions were performed concerning this effect.

Fig. 4(b) presents the load–deformation curves obtained experimentally. The unloading parts are omitted for clarity reasons. All curves start with linear elastic response up to a maximum load. The average maximum is  $F=206$  N. Following the peak there is stable crack propagation (in almost all cases and almost along the entire loading history). The data reduction scheme yields an average CERR of  $G_{\text{Ic}}=980$  J/m<sup>2</sup>, with a standard deviation of 11.5%. The response is similar to that known from DCB delamination tests justifying the choice of delamination tests for the determination of adhesive CERRs. Unfortunately the crack lengths have not been recorded (and it is not oblique in the applied standard), hence a resistance curve ( $R$ -curve) cannot be presented. It should thus be mentioned that the test method relies on the assumption that the  $R$ -curve is approximately constant along the range of crack lengths, and that the response

remains elastic within the laminate plates (which was the case in the performed experiments).

Investigating the failure locus is very important since the crack can switch from the adhesive to the adhesive/adherent interface or even into the composite plates. In such cases the fracture envelope would be an *effective* one since it lumps together the different phenomena. For this purpose the fracture surfaces were examined. A photograph of specimen 3 is exemplarily shown in Fig. 5(a). A failure locus in the middle of the adhesive layer is uniformly distributed over the entire fracture surface, except very small areas at the longitudinal edges, where the crack path switched into the composite. This is probably caused by edge splintering during the cutting of the specimens. In little cases the crack switched to the adhesive/laminate interface, see Fig. 5(b). However, we emphasize that the undesired failure loci occurred only in very localized areas and thus have a minor impact on the adhesive fracture toughness.

## 2.2. Single mode II

This section deals with the characterization of the single mode II CERR,  $G_{\text{IIc}}$ , via ENF tests. The test setup is illustrated in Fig. 6, which is a three point bending test on a pre-damaged specimen. The specimens are cut from the single mode I specimens after the

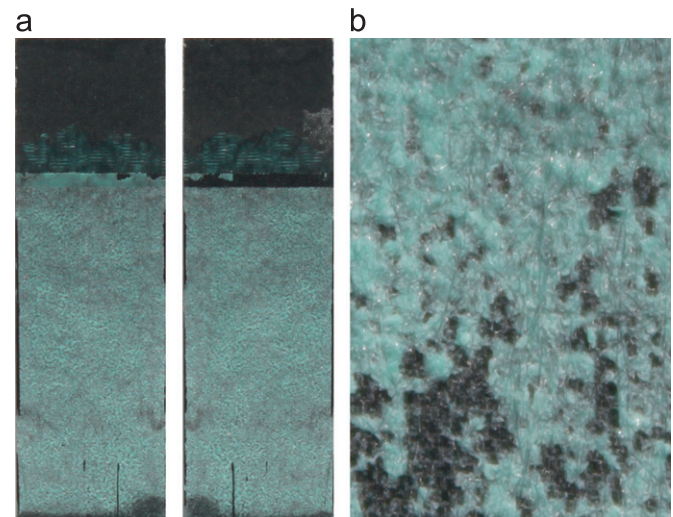


Fig. 5. Photographs of the fracture surfaces; specimen 3 (a) and detail of specimen 13 (b).

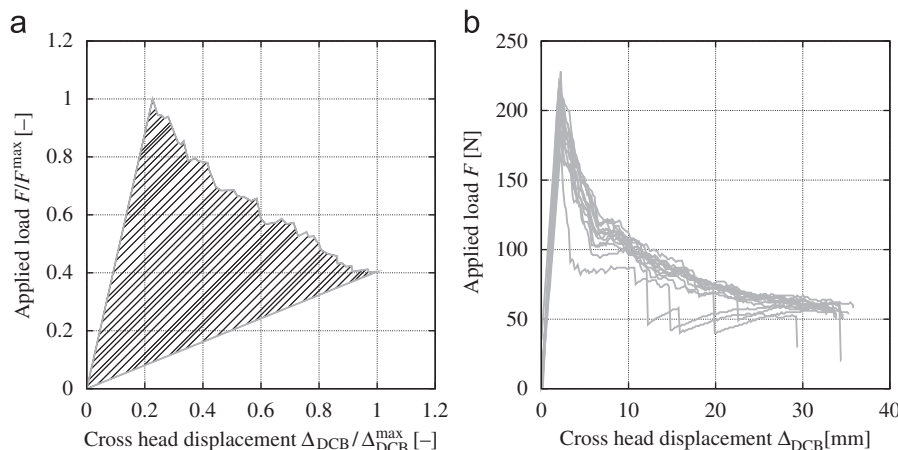
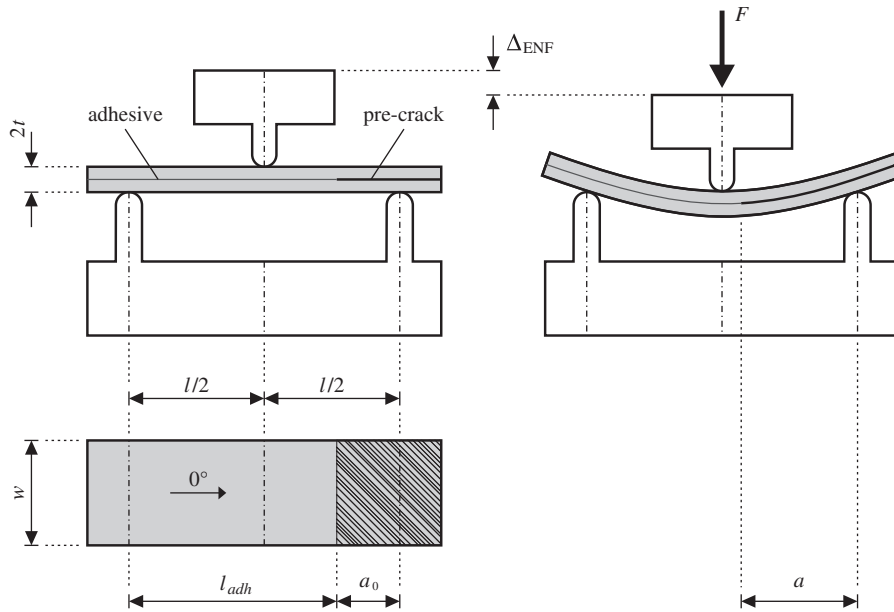


Fig. 4. Sketch of a typical DCB load–deformation curve (a) and own experimental results (b).





**Fig. 6.** Illustration of the ENF test setup and the specimen geometry (top left: initial configuration; bottom left: vertical projection of the test specimen; right: loaded configuration).

DCB tests. Consequently, the pre-damage is a single mode I crack, and a series of 14 specimens was tested. The lay-up and the thickness of the plates are the same as described in Section 2.1. The geometrical measures are also listed in Table 1. The initial and current crack lengths,  $a_0$  and  $a$ , are measured from the side support up to the crack front as indicated in Fig. 6. The applied load is denoted by  $F$ , and the deformation magnitude is the cross-head displacement denoted by  $\Delta_{\text{ENF}}$ .

The test procedure works as follows: the load is introduced displacement-controlled and quasi-statically with a displacement rate of 1 mm/min. The crack length is monitored by a vernier caliper utilizing a microscope with 15- to 25-fold magnification. A thin layer of white ink was applied to the longitudinal side faces of the specimens to facilitate this measurement. Load-displacement data are recorded for the entire duration of the tests. The crack tip is optically observed with the microscope to detect the onset of crack propagation. The critical load at onset of crack propagation,  $F^{\text{crit}}$ , is recorded and the loading is stopped as soon as crack propagation can be identified by a small drop in the load-displacement curve. The mode II CERR is then calculated using the expression

$$G_{\text{IIc}} = \frac{9F^{\text{crit}}\Delta_{\text{ENF}}^{\text{crit}}a_0^2}{2w(l^3/4 + 3a_0^3)} \cdot 1000, \quad (2)$$

according to the standard. Herein,  $\Delta_{\text{ENF}}^{\text{crit}}$  is the loading displacement corresponding to the critical load  $F^{\text{crit}}$ . The factor 1000 is a unit conversion factor which is included because  $a_0$ ,  $\Delta_{\text{ENF}}^{\text{crit}}$ ,  $w$ ,  $l$ , and  $F^{\text{crit}}$  are measured in mm and N, respectively, while the unit of  $G_{\text{IIc}}$  is J/m<sup>2</sup>.

Fig. 7(a) shows the experimental load-displacement curves, where the applied load  $F$  is plotted against the cross-head displacement  $\Delta_{\text{ENF}}$ . The mean value of the CERRs extracted from the experiments is  $G_{\text{IIc}} = 390 \text{ J/m}^2$ . This result seems to be questionable due to the following reasons: first, the single mode II CERR  $G_{\text{IIc}}$  is approximately 2.5 times smaller than the single mode I CERR  $G_{\text{Ic}}$ . In contrast  $G_{\text{IIc}}$  is usually much higher than  $G_{\text{Ic}}$  in co-cured 0°/0° interfaces, and there is no indication for adhesive connections to behave differently. Second, the standard deviation of 41.3% is very high. Third, the test has to be stopped if

a small load drop indicates the onset of crack propagation. Actually, a load drop is hard to realize in the curves of Fig. 7(a) (though crack initiation was identified by optical inspection and a first alteration of the crack front). Probably the experiments have been stopped too early, which is also a good explanation of the low CERR value. Finally it is doubtful that the experimental  $G_{\text{IIc}}$  value can be utilized for fitting a CERR criterion. It may rather be used as a curve fitting parameter instead. Anyway, it is clear that the absence of correct single mode II test data is a limitation in evaluating CERR criteria.

### 2.3. Mixed mode I/II

In the following the experimental determination of mixed mode I/II CERRs by MMB tests is discussed. The test setup as well as the specimen geometry are depicted in Fig. 8. The loading state in the specimens is a combination of mode I and mode II loading, introduced via aluminum blocks at the pre-damaged end (mode I) and the center roller (mode II), respectively. The mode mixture can be controlled by calibrating the loading arm length  $c$ . The nominal mode mixtures investigated in this work are  $\beta = 0.25$ ,  $\beta = 0.5$ , and  $\beta = 0.75$ . A series of seven specimens were tested for  $\beta = 0.25$ , while two series of eight specimens were tested for  $\beta = 0.5$  and  $\beta = 0.75$ , respectively. Except using aluminum blocks for the introduction of the mode I loading (instead of piano hinges), the test apparatus was manufactured according to appendix X2 of the test standard.

The composite plates of which the test specimens are fabricated have a [0°]<sub>14</sub> stacking sequence and a nominal thickness of 1.75 mm. The layer thickness is again  $t_l = 0.125 \text{ mm}$ . The PTFE insert exhibits a thickness no greater than 13 μm. The length of the pre-crack  $a_0$  (as well as the current crack length  $a$ ) is measured from the load line in the aluminum blocks at the predamaged end up to the crack front, as indicated in Fig. 8. The specimens were not pre-cracked to obtain crack initiation values of the CERRs which are free of fiber bridging (though fiber bridging did not occur for large crack lengths as well). Mean values of measured geometrical data such as the loading arm length  $c$ , the length of the intact adhesive area  $l_{\text{adh}}$ , the pre-crack length  $a_0$ , the specimen width  $w$ , and the thickness of the

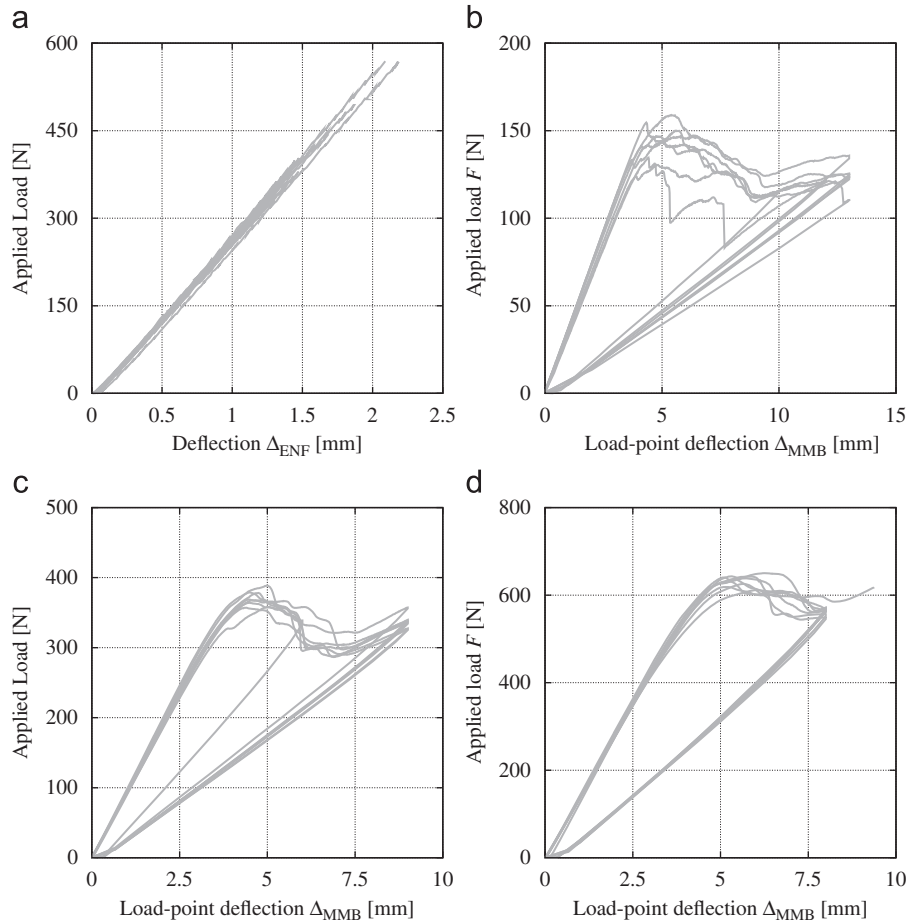


**Fig. 7.** Experimental load–deformation results of the ENF tests (a) and the MMB tests for mode mixing ratios of  $\beta = 0.25$  (b),  $\beta = 0.5$  (c), and  $\beta = 0.75$  (d). (a) Deflection  $\Delta_{ENF}$  (mm). (b) Load-point deflection  $\Delta_{MMB}$  (mm). (c) Load-point deflection  $\Delta_{MMB}$  (mm). (d) Load-point deflection  $\Delta_{MMB}$  (mm).

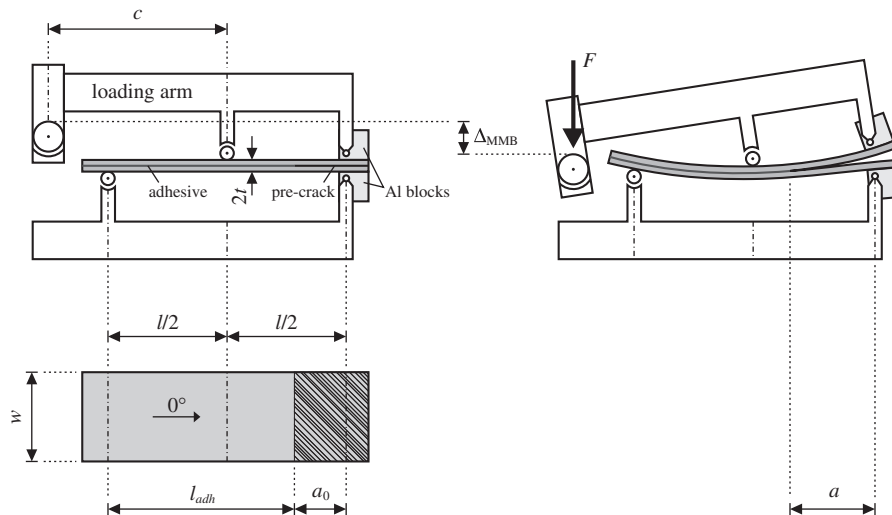


**Fig. 8.** Illustration of the MMB test setup and the specimen geometry (top left: initial configuration; bottom left: vertical projection of the test specimen; right: loaded configuration).

laminate plates  $t$ , are listed in Table 2. The loading arm length  $c$  was calibrated using the expression

$$c = \left( 0.167 + 0.000137 \tilde{a}^2 - 0.108 \sqrt{\ln(\tilde{a})} \beta^4 + \frac{-1400 + 0.725 \tilde{a}^2 - 141 \ln(\tilde{a}) - 302 \ln(\beta)}{219 - 5000 \beta + 55 \ln(\tilde{a})} \right) \frac{l}{2}, \quad (3)$$

**Table 2**

Geometrical data of the MMB test specimens (in mm).

$\beta$	$c$	$l_{adh}$	$a_0$	$w$	$t$
0.25	76.4	70.7	29.3	25.0	1.70
0.50	41.1	70.1	29.9	24.8	1.70
0.75	29.6	70.1	29.9	24.9	1.75

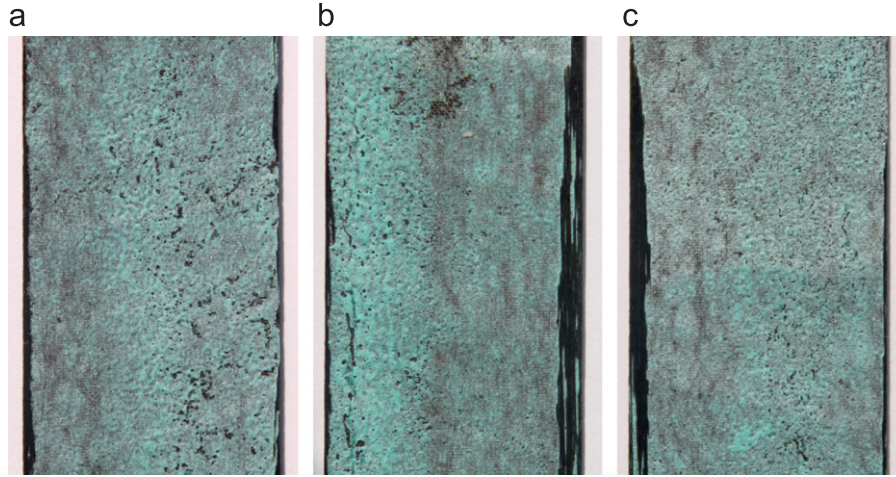


**Fig. 9.** Photographs of MMB fracture surfaces; specimen 6 with  $\beta = 0.25$  (a), specimen 7 with  $\beta = 0.5$  (b), and specimen 3 with  $\beta = 0.75$  (c) (crack propagation direction from top to bottom).

where  $\tilde{a} = a/t\chi$ . The parameter  $\chi$  is a crack length correction parameter defined by

$$\chi = \sqrt{\frac{E_{11}}{11G_{13}} \left[ 3 - 2 \left( \frac{\Gamma}{1 + \Gamma} \right)^2 \right]}, \quad (4)$$

and  $\Gamma = 1.18 \sqrt{E_{11}E_{22}/G_{13}}$  is a transverse modulus correction parameter. The material properties  $E_{11}$ ,  $E_{22}$ , and  $G_{13}$  were taken from preliminary experiments of project partners [32] and are given in Table 5. The compliance of the loading system was accounted for via the parameter  $C_{sys}$ , which was determined as described in Section 11.5 of the standard using a calibration specimen made of steel. The crack length correction parameter  $\chi$  is also utilized to calculate the stiffness of the laminate,  $E_{lf}$ , where also the system compliance enters:

$$E_{lf} = \frac{8(a_0 + \chi t)^3 \left( 3c - \frac{l}{2} \right)^2 + [6(a_0 + 0.43\chi t)^3 + 0.5l^3] \left( c + \frac{l}{2} \right)^2}{4l^2 b t^3 \left( \frac{1}{m} - C_{sys} \right)}. \quad (5)$$

Herein,  $m$  is the initial slope of the load–displacement curve by neglecting initial nonlinearities that may occur in the first 20% of the loading curve. The mode I and mode II strain energy release rates are obtained using the relationships

$$G_I = \frac{12 \left[ F \left( 3c - \frac{l}{2} \right) + F_g \left( 3c_g - \frac{l}{2} \right) \right]^2}{4b^2 t^3 l^2 E_{lf}} (a + \chi h)^2, \quad (6)$$

$$G_{II} = \frac{9 \left[ F \left( c + \frac{l}{2} \right) + F_g \left( c_g + \frac{l}{2} \right) \right]^2}{4b^2 t^3 l^2 E_{lf}} (a + 0.42\chi h)^2, \quad (7)$$

where  $F$  is the applied load,  $F_g$  is the weight of the loading lever and the attached apparatus, and  $c_g$  is the distance between the center of gravity and the center roller. A correction is thus included to take into account loading caused by the lever weight. Clearly,  $c_g$  changes with the lever load position. Note that Eqs. (3)–(7) are taken from the standard. The tests were performed displacement-controlled with a quasi-static displacement rate of 0.5 mm/min, where the controlled displacement is the cross-head displacement in the load line of the lever arm,  $\Delta_{MMB}$ , as seen in Fig. 8.

Fig. 7(b)–(d) shows the experimental load–displacement curves. We see that the initial response is linear elastic. At some point – characterized by the subscript ‘*nlin*’ in the following – the response starts to deviate from linearity and becomes non-linear.

**Table 3**

Experimental results of the MMB tests ( $F_{nlin}$  and  $F_{max}$  in N;  $G_{c,nlin}$  and  $G_{c,max}$  in J/m<sup>2</sup>;  $\sigma_{nlin}$  and  $\sigma_{max}$  in % related to the mean values).

$\beta$	$\beta_{nlin}$	$F_{nlin}$	$G_{c,nlin}$	$\sigma_{nlin}$	$\beta_{max}$	$F_{max}$	$G_{c,max}$	$\sigma_{max}$	$G_{c,max}/G_{c,nlin}$
0.25	0.2588	106	354	8.1	0.2558	146	658	10.6	1.89
0.50	0.5148	234	445	10.5	0.5116	370	1095	3.9	2.46
0.75	0.7412	345	529	36.6	0.7390	632	1683	4.4	3.18

At a later stage – denoted by the subscript ‘*max*’ in the following – the maximum load is reached followed by stable crack propagation. Unloading is almost linear to the origin, hence plasticity effects within the adhesive can be neglected. This qualitative response can be observed for all of the three mode mixing ratios.

The failure locus in all tests for all mode mixtures was somewhere in the adhesive layer, though the crack jumped to the adhesive/composite interface in some cases, and also into the composite plates in small stripes along the longitudinal side edges, as seen in Fig. 9. The latter effect is likely due to local damage caused by the cutting process and occurred only when the crack tip was far away from the initial crack tip, hence it has no influence on the initiation CERR values. The experimental outcome is useful for damage tolerance analyses since in real structures with realistic loading scenarios it can be expected that the failure locus is similar. However, the CERR has to be interpreted to be *effective*, since it lumps together different failure loci, and thus different failure mechanisms.

According to the standard [18] one has two options for the extraction of an initiation CERR. The first one is based on the load where the load–displacement curve first deviates from linearity,  $F_{nlin}$ . The second option is based on the maximum load,  $F_{max}$ . The related CERRs are denoted by  $G_{c,nlin}$  and  $G_{c,max}$ , respectively. The initiation CERRs are calculated as follows:

$$G_{c,nlin} = G|_{F_{nlin}, a_0} \quad \text{or} \quad G_{c,max} = G|_{F_{max}, a_0}. \quad (8)$$

Propagation values of the CERRs were not determined, thus the respective part of the standard is not described here. Also, since the crack lengths were not observed, *R*-curves of the MMB tests cannot be presented.<sup>2</sup> Table 3 lists the mean values of the initiation values of the CERRs calculated according to Eq. (8). The standard deviations related to the CERRs, namely  $\sigma_{nlin} = \sigma(G_{c,nlin})$

<sup>2</sup> Though it would be interesting to study if the CERRs are from the stable portion of the *R*-curve. Investigations on *R*-curves can be found e.g. in Ref. [33].



and  $\sigma_{max} = \sigma(G_{c,max})$ , are also given in Table 3. It may be mentioned that most of the standard deviations are pretty low. The difference between the nominal and the real mode mixing ratios is negligibly small, so we refer to the nominal values in the following. However, for completeness the real values are added in Table 3, where  $\beta_{nlin}$  is the real mode mixing ratio based on deviation from linearity and  $\beta_{max}$  is that based on the maximum load. The real mode mixities are obtained by applying Eqs. (6) and (7) in (1).

One can see from Table 3 that the CERRs and the load levels on which the extraction of the CERRs base increase significantly with increasing mode mixing ratio. One can also observe that  $G_{c,nlin}$  is significantly lower than  $G_{c,max}$ . The factor between the two CERR values increases with increasing mode mixing ratio starting from 1.89 for  $\beta = 0.25$  to 2.46 for  $\beta = 0.5$  and 3.18 for  $\beta = 0.75$ , see the last column of Table 3. This is an effect well-known for co-cured interfaces, which highlights that the response within an adhesive interface is very similar. The trend among the mixed mode CERRs seems to emphasize that the single mode II value from the ENF tests is not physically meaningful, so it will not be treated as a fix material parameter in the fit of CERR criteria, but as an additional fitting parameter.

For applications like damage tolerance analyses the question arises which CERR under mixed mode I/II conditions has to be used,  $G_{c,nlin}$  or  $G_{c,max}$ . The CERRs based on deviation from linearity are more conservative, but on the other hand may be too conservative. Furthermore, since the single mode I value ( $\beta = 0$ ) is 980 J/m<sup>2</sup> there is no monotonic trend in CERRs which is of course desired for fitting a CERR criterion. In order to reach a decision in this question, we apply a numerical approach in order to check which CERR is suitable for related failure analyses. The numerical approach is subject of the next section.

### 3. Numerical estimate

A numerical model is employed in this section which allows to verify which type of CERR to use,  $G_{c,nlin}$  or  $G_{c,max}$ . For this purpose we first describe the numerical approach used in this work, then validate the model on tests performed for co-cured interfaces, and then present the numerical estimate of the adhesive fracture toughness for the mode mixing ratios  $\beta = 0.25$ ,  $\beta = 0.5$ , and  $\beta = 0.75$ .

#### 3.1. Analysis approach

The specimens are subdivided into two sublaminae, of which each represents one half of the specimens, connected by an interface layer which describes the physical behavior of the adhesive. The sublaminae are modeled with quadrilateral layered shell elements. The interface is displayed by so-called interface elements in which a cohesive law is implemented accounting for the nonlinear damage behavior of the adhesive. The detailed derivation of the finite element formulations or the cohesive law are not subject of this paper, but the basic features are described in the sequel.

##### 3.1.1. Shell elements

The shell elements used for the simulations are state-of-the-art, so a detailed derivation of the element formulation is not given here. The element type is a quadrilateral iso-parametric plane shell with bi-linear Lagrangian shape functions. Geometrical nonlinearity is included by means of Green strains and second Piola–Kirchhoff stresses. The formulation holds for moderate rotations. Further the normal through-thickness strain and stress are neglected, which is a reasonable assumption for thin structures. The shell formulation builds upon a Reissner–Mindlin

kinematic. Therein, transverse shear is accounted for which usually poses problems related with locking effects. Transverse shear locking is eliminated by the well-known assumed natural strains (ANS) approach [34].

The layered formulation incorporates a transversely isotropic material law for each ply where the preferred direction is the fiber direction. An arbitrary stacking sequence can thus be described. The element also allows for an arbitrary choice of the reference surface which is essential for the connection with the interface elements. For the connection technique the reference surface is the bottom surface for the top sublaminate and vice versa for the bottom sublaminate. Offsets between the reference surface and the mid-surface of a particular ply are accounted for in the thickness integration scheme.

##### 3.1.2. Interface elements

The interface element formulation has been derived in detail in Refs. [35–37] and will not be repeated in this paper. The eight-node elements work in traction-separation relationships. The tractions are the interfacial tractions, which are the normal traction perpendicular to the interface,  $t_n$ , and the two shear tractions parallel to the interface,  $t_{II}$  and  $t_{III}$ . The single mode separations are denoted by  $\bar{u}_I$ ,  $\bar{u}_{II}$ , and  $\bar{u}_{III}$ . The separations are defined as the relative displacements between the top and the bottom sublaminate. Hence, the separations are obtained by simply subtracting the displacements of the bottom surface from the displacements of the top surface, of which each is approximated by bi-linear Lagrangian shape functions. It should be mentioned that the initial thickness of the interface is equal to zero. A similar element type has been used by several authors, see e.g. [38–46] among many others.

##### 3.1.3. Cohesive law

The cohesive law implemented in the interface element is a modified version of that proposed in [47,48]. Details about this model can be found in [35,49–51]. The model bases on the universal binding law of Rose et al. [52]. The original model from [47,48] is edited in a way that only tensile normal tractions or the shear tractions trigger damage within the interface, and not interfacial compression. A penalty contact formulation is added in order to avoid the interpenetration of cracked surfaces.

The resulting traction-separation laws for single mode I and II loading conditions are depicted in Fig. 10. The response in single mode III is qualitatively identical to that in mode II. It should be mentioned that for shearing the separation sign has no influence, whereas in mode I there is the softening behavior for tension and the contact behavior for compression. The peaks characterizing damage initiation are governed by the mode I and II strengths,  $R_I$  and  $R_{II}$ , and the corresponding separations,  $\bar{u}_I^0$  and  $\bar{u}_{II}^0$ . The points where the tractions revert to zero correspond with total decohesion. The areas under the traction-separation curves are defined as the CERRs. The parameter  $K$  denotes the penalty stiffness applied in the event of contact. In contrast to the nonlinear loading path unloading is linear to the origin as depicted in Fig. 10. This history-dependency avoids healing of the interface.

In order to account for mixed mode loading conditions an effective traction and an effective separation are introduced to generate a mode coupling yielding an effective traction-separation law<sup>3</sup>. The area under this effective traction-separation law is the mixed mode CERR. It should be mentioned that we assume

<sup>3</sup> For single mode loading conditions the effective traction-separation law is equal to the corresponding single mode traction-separation law as depicted in Fig. 10.

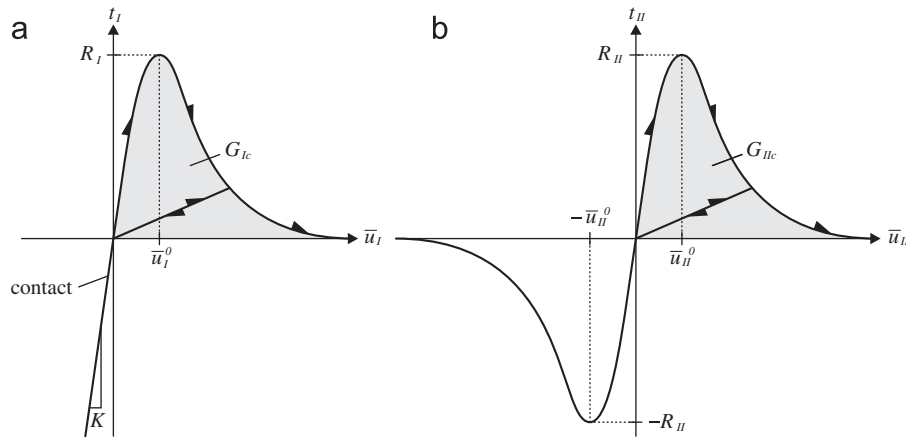


Fig. 10. Illustration of the single mode I (a) and single mode II (b) cohesive laws.

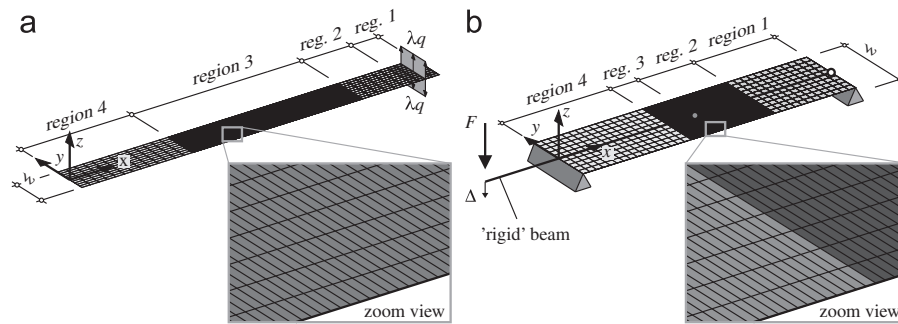


Fig. 11. Finite element meshes for the DCB test (a) and the MMB tests (b).

the same strengths for mode II and III. In [50] the smooth exponential cohesive law has been proven to be superior compared with a classical bi-linear model, as e.g. described in [53,54], in terms of computational stability and convergence behavior.

### 3.2. Validation with co-cured interfaces

In order to prove the capabilities of the analysis approach, and to motivate the choice of this approach for a numerical estimation of the CERRs in single mode I and mixed mode I/II loading conditions, DCB and MMB delamination tests with co-cured interfaces are simulated as validation examples. The DCB tests are reported in [55] and the MMB tests in [56]. Fig. 11 illustrates the finite element meshes used for the simulations.

In the DCB case, see Fig. 11(a), regions 1 and 2 are the areas where the pre-crack is located (16+29 mm long), region 3 is the region where cohesive interface elements are inserted (100 mm long), and region 4 is the remaining area where delamination is restricted (65 mm long). In region 4 only one layer of shell elements is used. The width of the specimen is  $w=20$  mm and the overall thickness of the laminate is  $2t=3$  mm. In contrast to Fig. 3 the load was introduced via aluminum blocks glued to the specimens according to the American standard ASTM D5528 [8]. The width of these was 16 mm, thus region 1 is 16 mm long. In order to account for the idealized rigid body motion of the aluminum blocks the elastic properties of the laminate in region 1 are chosen to 1000 times the original values. The parameter  $\lambda$  is a load factor which is computed by the applied displacement-controlled arclength procedure. Therein, the cross-head displacement is increased incrementally. The resultant of the applied load is defined by  $F=\lambda q w$  for every load step. The geometric boundary conditions are clamping of the end without pre-damage and fixing the rotations about the shell directors. The loaded nodes

are connected in z-direction via multiple point constraints (MPCs) which means that their displacements in z-direction are equal.

In the MMB case, see Fig. 11(b), region 1 is the pre-cracked area. Here, interface elements which only account for contact and not for cohesion are inserted since there is interfacial compression on a cracked surface. Regions 2 and 3 are the regions where the initial defect may grow. Here cohesive interface elements are inserted. Region 2 extends up to the middle of the specimen and region 3 is half as long as region 2. Region 4 is the area where delamination is restricted to grow. No interface elements are inserted here and only one layer of shell elements is used. The lengths of the particular regions depend on the length of the pre-crack which was measured after testing. For this purpose the specimens were separated in the delamination plane, and then the pre-crack length was measured. The mean values of the loading arm length  $c$ , the length of the intact adhesive region  $l_{adh}$ , the pre-crack length  $a_0$ , the width of the specimens  $w$ , the thickness of one sublaminate  $t$ , and the CERR for the three nominal mode mixing ratios are given in Table 4. The lengths of regions 1–4 can easily be computed by simple geometric considerations. The width of the specimens is  $w=25$  mm and the overall thickness is  $2t=4.2$  mm. The loading arm is modeled with a quasi-rigid beam which has a stiffness of 1000 times the laminate stiffness, hence rigidity is represented with sufficient accuracy. The beam is connected hinge-like with the upper sublaminate on the pre-cracked end, and is connected only in y- and z-directions with the upper sublaminate in the center of the specimen, see Fig. 11(b). In this point a connection in x-direction is omitted in order to avoid tension stiffening due to the bending process.

It should be mentioned that 200 elements are inserted in region 3 in the DCB case and 40+20 elements in regions 2 and 3 in the MMB case in longitudinal direction. This means a mesh

density of two elements per mm in the crack propagation regions, which is necessary for obtaining converged solutions.

The material properties taken for the laminate and the interface are listed in Table 5. These parameters have been determined

**Table 4**

Geometrical data (in mm) and CERR values (in J/m<sup>2</sup>) for the MMB tests with co-cured interfaces.

$\beta$	$c$	$l_{adh}$	$a_0$	$w$	$t$	$G_c$
0.25	76.4	70.4	29.6	25	2.1	344
0.50	41.1	69.6	30.4	25	2.1	514
0.75	29.6	68.9	31.1	25	2.1	981

**Table 5**

Material properties of the laminate and the interface (moduli and strengths in N/mm<sup>2</sup>, CERR in J/m<sup>2</sup>, the Poisson ratio is unit-free).

$E_{11}$	$E_{22}$	$\nu_{12}$	$G_{12} = G_{13} = G_{23}$	$R_I$	$R_{II}$	$G_{Ic}$
147,300	11,800	0.3	6000	51.0	115.7	270

experimentally by project partners within the COCOMAT project [57,58], see [32]. The  $G_{Ic}$  value is extracted from the DCB tests. Since for every computation the mixed mode CERR enters the cohesive law a single mode II CERR is not required for the simulations presented in this section. The mode I strength  $R_I$  is assumed to be equal to the in-plane strength of the laminate transverse to the fiber direction. The mode II strength  $R_{II}$  is the interlaminar shear strength (ILSS) determined via the American standard ASTM D2344 [59].

Fig. 12 presents the load–deformation curves of the DCB and MMB tests, that means for mode mixing ratios of  $\beta = 0$ ,  $\beta = 0.25$ ,  $\beta = 0.5$ , and  $\beta = 0.75$ , respectively. In the case of the DCB test, see Fig. 12 (a), the deformation magnitude is the cross-head displacement  $\Delta_{DCB}$ , whereas in the case of the MMB tests the deformation is the load-point deflection  $\Delta_{MMB}$ , see Fig. 12(b)–(d). One can see that for all of the four mode mixing ratios we obtain excellent agreement between numerical solution and experimental outcome. The initial stiffness, the maximum load, and the response in crack propagation are almost coincident. For the MMB simulations the experimentally determined CERR values are taken, see Table 4, which are reported in [56]. The high quality of these results validates the analysis approach for single mode I and mixed mode I/II loading conditions in co-cured interfaces, and justifies the choice of the approach for the numerical estimation of a

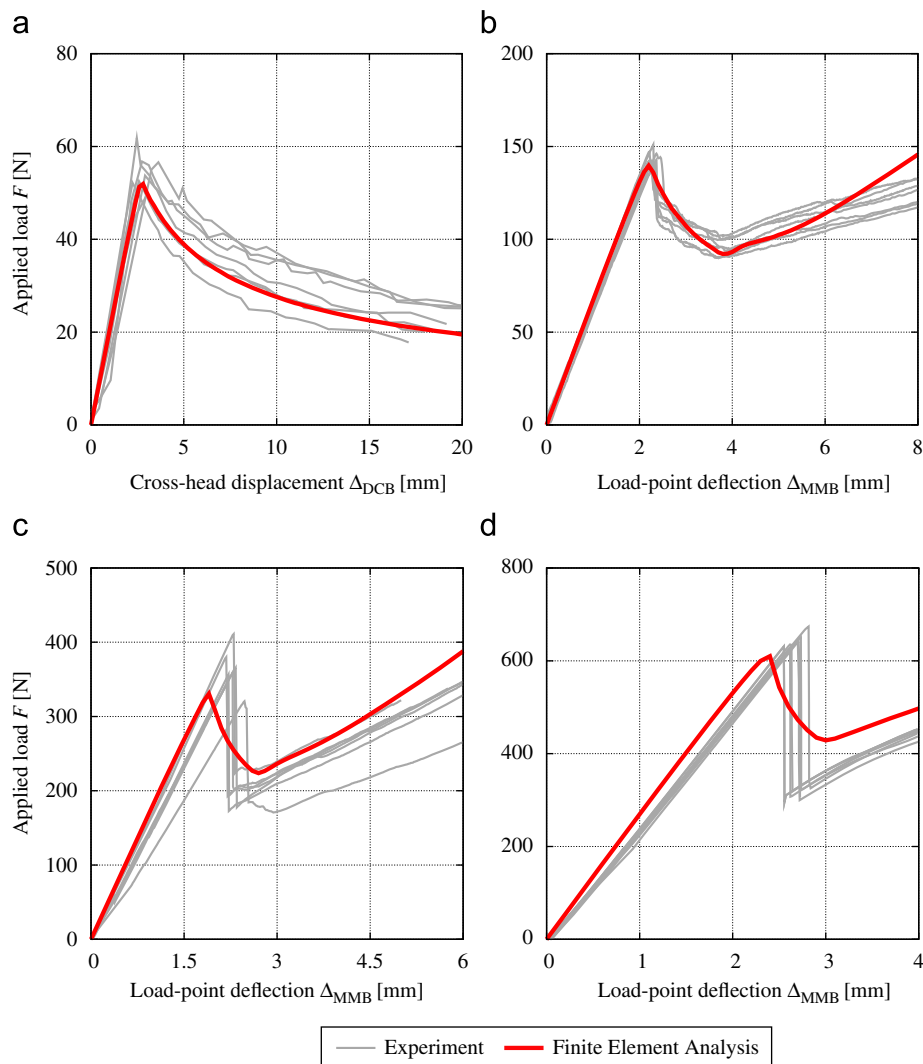


**Fig. 12.** Load–deformation curves of the delamination tests for mode mixing ratios of  $\beta = 0$  (a),  $\beta = 0.25$  (b),  $\beta = 0.5$  (c), and  $\beta = 0.75$  (d) (grey lines: test results; red lines: simulation).

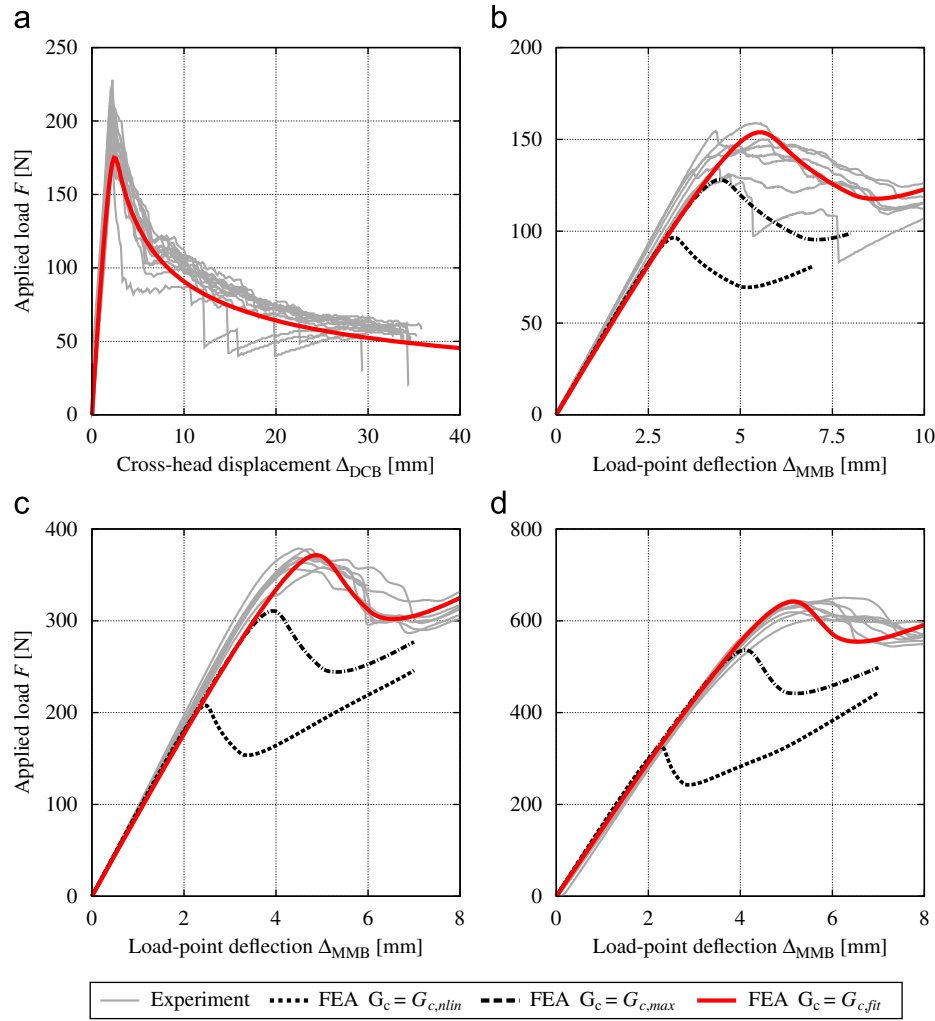


**Fig. 13.** Load–deformation curves of the adhesive fracture tests for mode mixing ratios of  $\beta = 0$  (a),  $\beta = 0.25$  (b),  $\beta = 0.5$  (c), and  $\beta = 0.75$  (d). (For interpretation of the references to color in this figure legend, the reader is referred to the web version of this article.)

suitable CERR for an adhesive interface, which is subject of the next section.

### 3.3. Adhesive fracture toughness

For the numerical estimation of adhesive CERRs the finite element meshes are principally identical to those from Section 3.2, see Fig. 11. However, in the DCB case the FE was introduced via piano hinges in the experiments and the FE version is discretized only up to where the resulting load acts. Thus region 1 does not exist and the load is introduced via a line load along the specimen width on the pre-cracked end. The geometrical data such as pre-crack length, intact adhesive length, width, and thickness of the specimens can be found in Table 1. Region 3, the area where the crack can propagate and where interface elements are inserted, is 120 mm long and is discretized with 240 elements in longitudinal direction, hence there are two elements per mm. In the MMB case the only differences between the FE mesh used in Section 3.2 and that used in this section are the geometrical data which are taken from Table 2 and not from Table 4. The elastic properties of the composite plies are those from Table 5. The interfacial strengths used for the analyses are  $R_I = 8 \text{ N/mm}^2$  and  $R_{II} = 40 \text{ N/mm}^2$ . These values originate from (unpublished) previous investigations, and are realized as reasonable numbers. Actually, they are curve-fits against experimental data. The CERRs are taken from the experiments,

i.e.  $G_{Ic} = 980 \text{ J/m}^2$  and  $G_c = G_{c,nlin}$  or  $G_c = G_{c,max}$ , with  $G_{c,nlin}$  and  $G_{c,max}$  from Table 3.

Fig. 13(a) shows the load–deformation curves of the simulation against the test results for the DCB test. Excellent agreement can be observed in terms of initial stiffness, maximum load, and crack propagation stiffness. We conclude that the  $G_{Ic}$  value from the DCB tests is a reasonable estimate, thus fitting is not necessary.

Fig. 13(b)–(d) present the load–deformation curves of the MMB adhesive tests and the respective finite element analyses (FEA). Only the loading paths are plotted in these pictures. The black dashed and dot-dashed curves are the results of the FEA with  $G_{c,nlin}$  and  $G_{c,max}$ , respectively. One can see that none of these yields correlation with the experiments for all of the three investigated mode mixing ratios. The maximum loads and the response in crack propagation, i.e. the decreasing paths after the maximum load, are significantly under-estimated. It seems that neither the CERR based on the point of deviation from linearity nor that based on the maximum load apply for an adhesive fracture toughness. Clearly speaking, the initiation CERR values appear to be much too low.<sup>4</sup> Maybe propagation values extracted according to Section 5.3.2 of the standard [18] are more

<sup>4</sup> The effect of a too low fracture toughness can also be seen in Fig. 1.

**Table 6**  
CERR values from the numerical estimate (in J/m<sup>2</sup>).

$\beta$	0.00	0.25	0.50	0.75
$G_{c,fit}$	980	990	1650	2600

reasonable, especially because they are expected to be larger than the initiation values, but these were not determined in the framework of this work. Thus we tried a numerical estimate of the CERRs by trial-and-error fits until the finite element results converged to the experiments. The respective CERRs are denoted by  $G_{c,fit}$  and are given in Table 6. The corresponding curves are plotted as solid red lines in Fig. 13(b)–(d) and show very good agreement with the test curves. Initial stiffness, maximum load, and crack propagation stiffness almost coincide.

The fact that the numerical model can be calibrated to the experimental outcome validates the analysis approach for applications to adhesive joints. The CERRs obtained via the numerical fit in the MMB case, and that obtained via experimental testing in the DCB case, seem to be the right choice for numerical applications and are used as the *real* values for fitting a CERR criterion. It should be mentioned that we do not provide numerical results for the ENF tests since we do not have the crack propagation paths available for comparison.

#### 4. Fracture toughness criteria

This section deals with the evaluation and validation of suitable fracture toughness criteria available from the literature. The basis for fitting these criteria are the CERR values for specific mode mixing ratios which have been obtained directly via experiments for  $\beta = 0$  or indirect by the semi-numerical estimate as described previously for  $\beta = 0.25$ ,  $\beta = 0.5$ , and  $\beta = 0.75$ . The fracture toughness for the single mode II case,  $G_{IIc}$ , is used as a fitting parameter. In this section we first review some of the available criteria for mixed mode I/II scenarios, then present the results of least squares fits against the basic values deduced in Section 3.3, and then present a simple approach to include mode III behavior which is based on some basic assumptions.

##### 4.1. Review of available criteria

Several criteria have been applied in the past, ranging from power laws with uniform or different exponents for mode I and II over polynomial criteria to the one proposed by Benzeggagh and Kenane [60], which is referred to as the *BK-criterion* in the following. Surveys on available criteria can be found e.g. in [6,61]. An extract of these are reviewed in the sequel. Let us first consider that the most general fracture-mechanics-based criterion for crack propagation is that the total energy release rate  $G_T$ , which is defined as the sum of the single mode energy release rates, is equal to the mixed mode CERR. This criterion reads

$$G_c = G_I + G_{II} = G_T \Leftrightarrow \frac{G_T}{G_c} = 1. \quad (9)$$

The most easy imaginable mode interaction criterion is that there is no interaction at all. In this case the fracture toughness remains unchanged when altering the mode mixing ratio. However, such a criterion is evidently wrong and is not considered here. Another simple interaction criterion is a power law. The most general power law from which some other criteria can be deduced is

defined by

$$\left(\frac{G_I}{G_{Ic}}\right)^{\alpha_1} + \left(\frac{G_{II}}{G_{IIc}}\right)^{\alpha_2} = 1, \quad (10)$$

see [62]. A wide range of material response can be displayed with this criterion by choosing any combination of  $\alpha_1$  and  $\alpha_2$  [63,64]. If equal values  $\alpha_1 = \alpha_2 = 1$  are utilized we obtain the linear interaction

$$\frac{G_I}{G_{Ic}} + \frac{G_{II}}{G_{IIc}} = 1. \quad (11)$$

Substitution of (1) and (9) and some basic mathematical manipulations yield an expression for the mixed mode CERR in terms of the mode mixing ratio:

$$G_c = \left(\frac{1-\beta}{G_{Ic}} + \frac{\beta}{G_{IIc}}\right)^{-1}. \quad (12)$$

A linear interaction of the different failure modes may not be sufficient for an accurate representation of the mixed mode CERR. For a quadratic interaction we have to set  $\alpha_1 = \alpha_2 = 2$  so we obtain

$$\left(\frac{G_I}{G_{Ic}}\right)^2 + \left(\frac{G_{II}}{G_{IIc}}\right)^2 = 1. \quad (13)$$

Again substituting (1) and (9) leads to an expression for the mixed mode CERR in terms of the mode mixing ratio which is given by

$$G_c = \left[\left(\frac{1-\beta}{G_{Ic}}\right)^2 + \left(\frac{\beta}{G_{IIc}}\right)^2\right]^{-1/2}. \quad (14)$$

The same methodology can be used for deducing a more general power law which includes (12) and (14). For this purpose we set  $\alpha_1 = \alpha_2 = \alpha$  and we obtain

$$G_c = \left[\left(\frac{1-\beta}{G_{Ic}}\right)^\alpha + \left(\frac{\beta}{G_{IIc}}\right)^\alpha\right]^{-1/\alpha}. \quad (15)$$

Besides the power laws described previously Yan et al. [65] proposed a second order polynomial as a CERR criterion. The original criterion was formulated in terms of a mode mixing ratio defined by  $\hat{\beta} = G_{II}/G_I$ . Since in the event of mode-II-dominated scenarios  $G_I \rightarrow 0$ , and as a consequence  $\hat{\beta} \rightarrow \infty$ , Reeder [6] rated this criterion as inappropriate. A modification has been reported in [66] where a mode mixing ratio enters according to the definition given in (1). This transformation yields a polynomial criterion given by

$$G_c = G_{Ic} + \mu_1 \beta + \mu_2 \beta^2, \quad (16)$$

which is now comparable with the power laws given above. The polynomial covers a wide range of material response and is able to approximate both concave and convex models. Another criterion which attained much attention is the BK-criterion [60]:

$$G_c = G_{Ic} + (G_{IIc} - G_{Ic})\beta^\eta. \quad (17)$$

It may be mentioned that in our case all of the above-mentioned criteria have the same amount of curve fitting parameters. The general power law given by (15) contains the exponent  $\alpha$  and  $G_{IIc}$ , the polynomial (16) contains the coefficients  $\mu_1$  and  $\mu_2$ , and the BK-criterion (17) contains the exponent  $\eta$  and  $G_{IIc}$ . Several criteria have been proposed in addition to the above-mentioned ones, see e.g. [67–70] among others, but these are not addressed in this paper.

##### 4.2. Least squares fit

In this section a least squares fit of most of the CERR criteria described in the previous section is presented. For the fitting the software package gnuplot [71] was utilized. We did not obtain a converged solution when we tried to fit the power law from



Eq. (15), thus we used the linear and the quadratic power laws, see (12) and (14), and in excess to these also a power law with an exponent of  $\alpha = 4$ . The results of the fits are plotted in Fig. 14.

One principally expects a monotonic trend in the CERR values. With increasing mode mixing ratio the CERR should also increase. Further the outcome of the single mode II CERR, which is a fitting parameter, should be as low as possible so that simulations under pure shear loadings do not overestimate the physical response.

The postulation for a monotonically increasing trend with increasing mode mixing ratios is not true for the CERRs based on the point of deviation from linearity or on the maximum load, see Fig. 14(a) and (b), and thus also not for most of the corresponding criteria fits. In the case of the  $G_{c,nlin}$  values the power laws show a decreasing trend which makes no sense from a physical point of view. The polynomial first decreases up to  $\beta \approx 0.4$  and then increases for higher mode mixing ratios, which also makes no sense. Fitting the BK-criterion did not converge because it cannot display decreasing values of the CERRs for increasing mode mixing ratios. In the case of the CERRs based on the maximum load the discrete value for  $\beta = 0.25$  violates a monotonic trend. The best fit against the  $G_{c,max}$  values is obtained for the second order polynomial. However, in the range of  $\beta < 0.25$  the curve decreases and with further increasing mode mixing ratio it increases, hence there is no monotonic trend. The BK-criterion increases monotonically, but due to that yields no good approximation of the CERR for  $\beta = 0.25$ . The power law with  $\alpha = 1$  exhibits a monotonically increasing behavior but has a large error at the discrete CERR

values. The decreasing behavior of the power laws with  $\alpha = 2$  and  $\alpha = 4$  for  $\beta > 0.6$  and  $\beta > 0.5$  is physically doubtful.

The discrete values of the CERRs based on the numerical estimate,  $G_{c,fit}$ , exhibit a monotonically increasing trend, and so do the criteria fits except the power laws with  $\alpha = 2$  and  $\alpha = 4$ . The fit with the lowest error norm is obtained with the second order polynomial, which is also the only criterion which displays the mild decrease in fracture toughness for very low mode mixing ratios.

The BK-criterion and the power law with  $\alpha = 1$  have a monotonic trend for all mode mixing ratios. However, the BK-criterion has a lower error norm and yields a lower  $G_{IIc}$ , and is thus rated as the better criterion for the determination of the adhesive mixed mode CERR. Since the polynomial and the BK-criterion exhibit very similar shapes, we give both parameter sets which are

$$\mu_1 = -946.15 \text{ kJ/m}^2, \quad \mu_2 = 4246.55 \text{ kJ/m}^2, \quad G_{IIc} = 4280.40 \text{ kJ/m}^2, \quad (18)$$

for the polynomial, and

$$G_{Ic} = 980 \text{ kJ/m}^2; \quad G_{IIc} = 4562 \text{ kJ/m}^2; \quad \eta = 2.63, \quad (19)$$

for the BK-criterion. From a physical point of view – concerning especially the presence of a monotonic increase in CERRs for increasing mode mixing ratios – we rate the BK-criterion as most appropriate for the prediction of mixed mode CERRs.

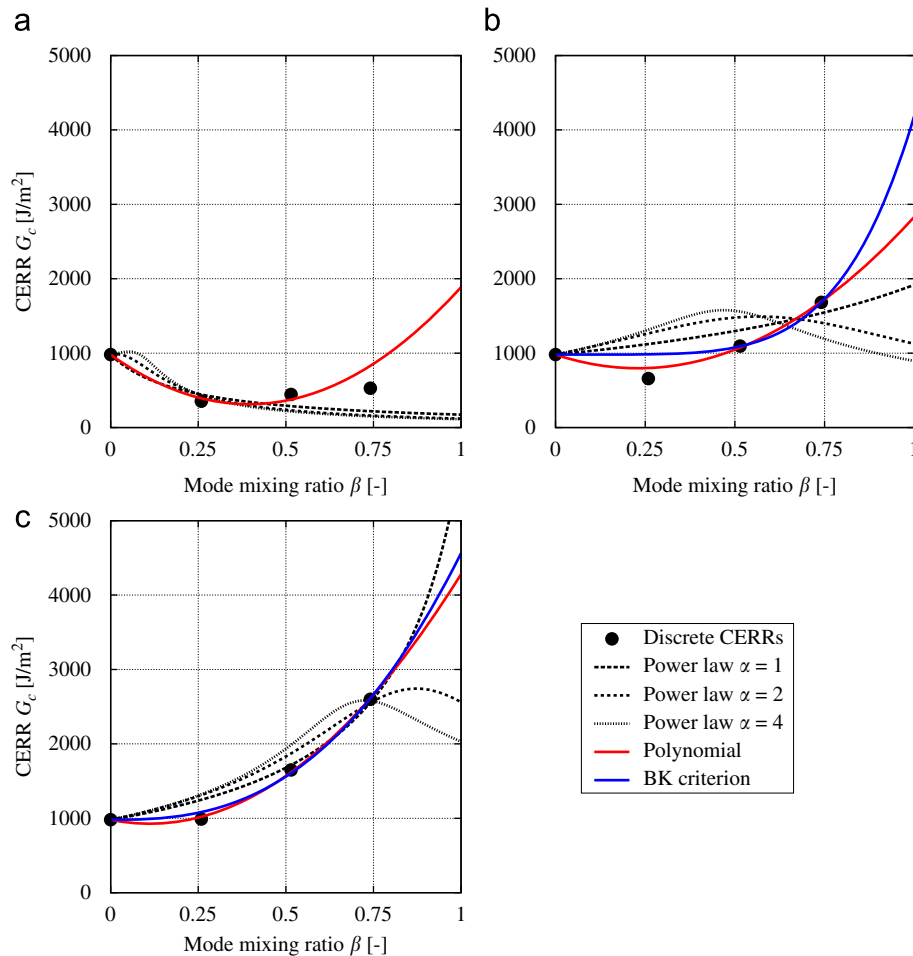


**Fig. 14.** Plots of the CERR criteria fitted against  $G_{c,nlin}$  (a),  $G_{c,max}$  (b), and  $G_{c,fit}$  (c). (For interpretation of the references to color in this figure legend, the reader is referred to the web version of this article.)

#### 4.3. Inclusion of mode III

In the CERR criteria previously reviewed, mode III response does not enter since there is no standardized test method available which incorporates mode III. However, promising work has been done in the past concerning the experimental characterization of the single mode III CERR. For instance, Donaldson [72] proposed the split cantilever beam (SCB) test on which Martin [73] performed fundamental work for its evaluation. Another method, which experienced more attention, is the edge crack torsion (ECT) test which has been developed by Lee [74]. Unfortunately, the ECT test is in discussion since a certain portion of mode II loading is introduced into the interface which is hard to capture in data reduction schemes. Due to this lack of experimental evidence we can only guess how to respect mode III influences. The following is a proposal on how to proceed in mixed mode I/II/III loading conditions by extending the BK-criterion.

Following the work of Li [75] we introduce a total shear energy release rate  $G_{shear}$  as

$$G_{shear} = G_{II} + G_{III}, \quad (20)$$

and we redefine the total energy release rate  $G_T$

$$G_T = G_I + G_{shear}. \quad (21)$$

Camanho and Dávila [53] assume the same CERRs for mode II and mode III, i.e.  $G_{IIc} = G_{IIIc}$ . Then in the mixed mode I/II criteria from Section 4.1 the single mode II energy release rate  $G_{II}$  can be replaced by the total shear energy release rate  $G_{shear}$  while the mode mixing ratio reads  $\beta = G_{shear}/G_T$  in this case.

However, this assumption stands in contrast to the publication of Lee [74] who found that in mode III the CERR is usually higher than that in mode II. Hence, an easy approach to find a more realistic shear fracture toughness  $G_{c,shear}$  is to assume a quadratic interaction between the shear modes and to construct an elliptic fracture toughness envelope as depicted in Fig. 15.

The elliptic criterion, or quadratic power law, reads

$$\left(\frac{G_{II}}{G_{IIc}}\right)^2 + \left(\frac{G_{III}}{G_{IIIc}}\right)^2 = 1. \quad (22)$$

Introducing a shear mode mixing ratio  $\beta_{shear} = G_{II}/G_{III}$ , and utilizing the relationship  $G_{c,shear} = (G_{II}^2 + G_{III}^2)^{1/2}$  for the total shear energy release rate, leads to

$$G_{c,shear} = G_{IIc}G_{IIIc} \sqrt{\frac{1 + \beta_{shear}^2}{G_{IIc}^2 + (\beta_{shear}G_{IIIc})^2}}, \quad (23)$$

as an expression for the total shear fracture toughness which now serves to replace the single mode II fracture toughness  $G_{IIc}$  in the criteria from Section 4.1. Again, the single mode II energy release rate  $G_{II}$  has to be replaced by the total shear energy release rate

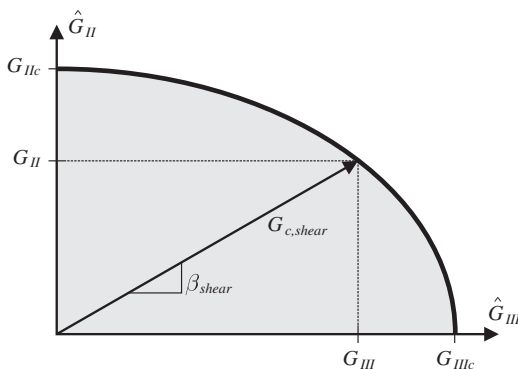


Fig. 15. Illustration of the elliptic envelope for the shear CERR  $G_{c,shear}$ .

$G_{shear}$  and the mode mixing ratio has to be defined as the ratio between the total shear energy release rate  $G_{shear}$  and the total energy release rate  $G_T$ . For the BK-criterion this method exemplarily yields

$$G_c = G_{IIc} + (G_{c,shear} - G_{IIc})\beta^n, \quad (24)$$

where  $G_{c,shear}$  is taken from Eq. (23) and  $\beta = G_{shear}/G_T$ . The authors emphasize that this approach is an assumption and is not validated through experimental investigations. Actually, it is presently not possible to validate this approach since there is no mixed mode I/II/III test method available. Also the single mode III CERR has to be determined by experiments which has not been done in the framework of this paper. As long as experimental data are not available for single mode III the assumption of equal CERRs for single mode II and III may be a reasonable approximation.

#### 5. Conclusions

In this paper a combined numerical/experimental approach was presented for the determination of the mixed mode critical energy release rate of adhesive joints in composite laminates. The material under investigation was a unidirectional Hexcel IM7/8552 carbon/epoxy composite which was connected by the film adhesive Cytec FM 300 M.

Experimental investigations have been carried out including classical delamination tests such as double cantilever beam, end notched flexure, and mixed mode bending tests where the co-cured interface was replaced by an adhesive bond. The experimental outcome was presented by means of global load-deformation curves and provides an important database for single mode I, single mode II, and mixed mode I/II loading conditions. Since in the MMB case it was not clear which initiation fracture toughness is useful for failure analyses, numerical simulations were performed in the framework of the finite element method, including state-of-the-art shell elements for the composite layers and interface elements with an embedded cohesive law for the adhesive. The numerical approach was first validated on simulations with co-cured interfaces before the results of the adhesive simulations were presented. Unfortunately, utilizing the CERRs from the experiments did not yield correlation with the tests. Thus the finite element simulations were fitted against the experiments by trial-and-error variation of the CERR values. These values were then interpreted as the real CERRs. Since the CERR is different for different mode mixing ratios fracture toughness criteria from the literature were evaluated and fitted against the CERR values for the mode mixing ratios under investigation. This led to mathematical expressions which gave the CERR as a function of the mode mixing ratio. The best fit in combination with physical plausibility was obtained for the so-called BK-criterion [60]. Finally, a simple method for including mode III behavior was described which relies on some basic assumptions.

The relation between the fracture toughness and the mode mixing ratio is the key outcome of this paper. It is important to know that the CERR is the major material parameter characterizing the fracture process within an adhesive. Hence, this paper forms a useful basis for failure analyses of a respective adhesive joint. This is exceptionally true as the investigated materials are standard in the aircraft industry. The specific results now have to be validated on more complex structures before final proof of their quality.

#### Acknowledgments

The authors kindly acknowledge the financial support of the European Commission, Priority Aeronautics and Space, Contract

AST3-CT-2003-502723. The authors further gratefully acknowledge the fruitful cooperation with all partners involved in the COCOMAT project [57,58].

## References

- [1] Campbell FC. Manufacturing processes for advanced composites. Kidlington, Oxford, United Kingdom: Elsevier Ltd.; 2004. ISBN 1856174158.
- [2] O'Brien TK. Fracture mechanics of composite delamination. In: Miracle DB, Donaldson SL, Henry SD, editors. Composites of ASM handbook, vol. 21. ASM International; 2001. p. 241–5. ISBN 978-0871707031.
- [3] Krüger R. Virtual crack closure technique: history, approach, and applications. Appl Mech Rev 2004;57(2):109–43. doi:10.1115/1.1595677.
- [4] Fernlund G, Spelt JK. Mixed-mode fracture characterization of adhesive joints. Compos Sci Technol 1994;50(4):441–9. doi:10.1016/0266-3538(94)90052-3.
- [5] Ducept F, Davies P, Gamby D. Mixed mode failure criteria for a glass/epoxy composite and an adhesively bonded composite/composite joint. Int J Adhes Adhes 2000;20(3):233–44. doi:10.1016/S0143-7496(99)00048-2.
- [6] Reeder JR. An evaluation of mixed-mode delamination failure criteria. Technical memorandum TM-1992-104210. Hampton, Virginia 23665-5225, USA: NASA, Langley Research Center; 1992.
- [7] Hansen P, Martin R. DCB, 4ENF and MMB delamination characterization of S2/8552 and IM7/8552. Technical report. Hertford, UK: Materials Engineering Research Laboratory Ltd. (MERL). Technical report N68171-98-M-5177; 1999.
- [8] ASTM Standard D5528-01(2007)e1. Standard test method for mode I interlaminar fracture toughness of unidirectional fiber-reinforced polymer matrix composites. West Conshohocken, PA, USA: American Society for Testing and Materials; 2007.
- [9] DIN Standard DIN EN 6033. Aerospace series—carbon fibre reinforced plastics—test method—determination of interlaminar fracture toughness energy—mode I— $G_{Ic}$ . Responsible committee NA 131-02-01 AA. Berlin, Germany: Deutsches Institut für Normung; 1996.
- [10] ISO Standard 15024:2001. Fibre-reinforced plastic composites—determination of mode I interlaminar fracture toughness,  $G_{Ic}$ , for unidirectionally reinforced materials. Geneva, Switzerland: International Organization for Standardization; 2001.
- [11] JSA Standard JIS K 7086. Testing methods for interlaminar fracture toughness of carbon fibre reinforced plastics. Tokyo, Japan: Japanese Standards Association; 1993.
- [12] DIN Standard DIN EN 6034. Aerospace series—carbon fibre reinforced plastics—test method—determination of interlaminar fracture toughness energy—mode II— $G_{IIc}$ . Responsible committee NA 131-02-01 AA. Berlin, Germany: Deutsches Institut für Normung; 1996.
- [13] Crews JH, Reeder JR. A mixed-mode bending apparatus for delamination testing. Technical report no. TM-100662. Hampton, Virginia, USA: NASA—National Aeronautics and Space Administration, Langley Research Center; 1988.
- [14] Reeder JR, Crews JH. Mixed-mode bending method for delamination testing. AIAA J 1990;28(7):1270–6.
- [15] Reeder JR, Crews JH. Nonlinear analysis and redesign of the mixed-mode bending delamination test. Technical report no. TM-102777. Hampton, VI, USA: NASA—National Aeronautics and Space Administration, Langley Research Center; 1991.
- [16] Reeder JR, Crews JH. Redesign of the mixed-mode bending delamination test to reduce nonlinear effects. J Compos Technol Res 1992;14(1):12–9.
- [17] Reeder JR. Refinements to the mixed-mode bending test for delamination toughness. J Compos Technol Res 2003;25(4):1–5. paper ID CTR11949.
- [18] ASTM Standard D6671-01. Standard test method for mixed mode I-mode II interlaminar fracture toughness of unidirectional fiber reinforced polymer matrix composites. West Conshohocken, PA, USA: American Society for Testing and Materials; 2001.
- [19] ISO Standard 25217:2009. Adhesives—determination of the mode I adhesive fracture energy of structural adhesive joints using double cantilever beam and tapered double cantilever beam specimens. Geneva, Switzerland: International Organization for Standardization; 2009.
- [20] Blackman BRK, Dear JP, Kinloch AJ, MacGillivray H, Wang Y, Williams JG, Yayla P. The failure of fibre composites and adhesively bonded fibre composites under high rates of test (Part I: mode I loading—experimental studies). J Mater Sci 1995;30(23):5885–900.
- [21] Blackman BRK, Kinloch AJ, Wang Y, Williams JG. The failure of fibre composites and adhesively bonded fibre composites under high rates of test (Part II: mode I loading—dynamic effects). J Mater Sci 1996;31(17):4451–66.
- [22] Blackman BRK, Dear JP, Kinloch AJ, MacGillivray H, Wang Y, Williams JG, Yayla P. The failure of fibre composites and adhesively bonded fibre composites under high rates of test (Part III: mixed mode I/II and mode II loadings). J Mater Sci 1996;31(17):4467–77.
- [23] Blackman BRK, Kinloch AJ, Rodriguez Sanchez FS, Teo WS, Williams JG. The fracture behaviour of structural adhesives under high rates of testing. Eng Fract Mech 2009;76(18):2868–89. doi:10.1016/j.engfracmech.2009.07.013.
- [24] Cho J-U, Kinloch A, Blackman B, Rodriguez S, Cho C-D, Lee S-K. Fracture behaviour of adhesively-bonded composite materials under impact loading. Int J Precis Eng Manufact 2010;11(1):89–95. doi:10.1007/s12541-010-0011-6.
- [25] Blackman BRK, Kinloch AJ, Paraschi M, Teo WS. Measuring the mode I adhesive fracture energy,  $G_{Ic}$  of structural adhesive joints: the results of an international round-robin. Int J Adhes Adhes 2003;23(5):293–305. doi:10.1016/S0143-7496(03)00047-2.
- [26] Blackman BRK, Johnsen BB, Kinloch AJ, Teo WS. The effects of pre-bond moisture on the fracture behaviour of adhesively-bonded composite joints. J Adhes 2008;84(3):256–76. doi:10.1080/00218460801954391.
- [27] Charalambides MN, Hardouin R, Kinloch AJ, Matthews FL. Adhesively-bonded repairs to fibre-composite materials I: experimental. Compos Part A: Appl Sci Manufact 1998;29A(11):1371–81. doi:10.1016/S1359-835X(98)00060-8.
- [28] Charalambides MN, Kinloch AJ, Matthews FL. Adhesively-bonded repairs to fibre-composite materials II: finite element modelling. Compos Part A: Appl Sci Manufact 1998;29A(11):1383–96. doi:10.1016/S1359-835X(98)00061-X.
- [29] Dillard DA, Singh HK, Pohlit DJ, Starbuck JM. Observations of decreased fracture toughness for mixed mode fracture testing of adhesively bonded joints. J Adhes Sci Technol 2009;23(10–11):1515–30. doi:10.1163/156856109X452701.
- [30] Cytec—Engineered materials, FM 300 high shear strength modified epoxy adhesive. Technical datasheet. Havre de Grace, MD, USA: Cytec Engineered Materials Inc.; Mar. 2005. URL <http://www.cytec.com>.
- [31] Hexcel Corp, HexPly 8552 Epoxy Matrix—Product Data, HEXCEL Corporation; Oct. 2008. URL <http://www.hexcel.com>.
- [32] COCOMAT Technical Report. Deliverable D03—characterization of material properties. Technical report; 2006.
- [33] Azari S, Eskandarian M, Papini M, Schroeder JA, Spelt JK. Fracture load predictions and measurements for highly toughened epoxy adhesive joints. Eng Fract Mech 2009;76(13):2039–55. doi:10.1016/j.engfracmech.2009.05.011.
- [34] Dvorkin EN, Bathe K-J. A continuum mechanics based four-node shell element for general non-linear analysis. Eng Comput 1984;1(1):77–88. doi:10.1108/eb023562.
- [35] Balzani C, Wagner W. Simulation of skin-stiffener debonding in stiffened carbon/epoxy panels. Proc Appl Math Mech 2007;7:4060019–20. doi:10.1002/pamm.200700253.
- [36] Balzani C, Wagner W. Numerical treatment of damage propagation in axially compressed composite airframe panels. Int J Struct Stab Dyn 2010;10(4):683–703. doi:10.1142/S0219455410003683.
- [37] Wagner W, Balzani C. Finite element modeling of stringer-stiffened fiber reinforced polymer structures. In: Kuczma M, Wilmanski K, editors. Computer methods in mechanics. Lectures of the CMM 2009 of advanced structured materials, vol. 1. Berlin, Heidelberg: Springer; 2010. p. 505–23. Chapter 27, ISBN 978-3642052408.
- [38] Needleman A. An analysis of tensile decohesion along an interface. J Mech Phys Solids 1990;38(3):289–324. doi:10.1016/0022-5096(90)90001-K.
- [39] Needleman A. An analysis of decohesion along an imperfect interface. Int J Fract 1990;42(1):21–40. doi:10.1007/BF00018611.
- [40] Allix O, Ladevèze P. Interlaminar interface modeling for the prediction of delamination. Compos Struct 1992;22(4):235–42. doi:10.1016/0263-8223(92)90060-P.
- [41] Tvergaard V, Hutchinson JW. The relation between crack growth resistance and fracture process parameters in elastic-plastic solids. J Mech Phys Solids 1992;40(6):1377–97. doi:10.1016/0022-5096(92)90020-3.
- [42] Rinderknecht S, Kröplin B. Calculation of delamination growth with fracture and damage mechanics. In: Hughes TJR, Oñate E, Zienkiewicz OC, editors. Recent developments in finite element analysis—a book dedicated to Robert L. Taylor. Barcelona, Spain: CIMNE; 1994. p. 181–90. ISBN 8487867456.
- [43] Crisfield M, Mi Y, Davies GAO, Hellweg HB. Finite element methods and the progressive failure-modelling of composite structures. In: Owen DRJ, Oñate E, Hinton E, editors. Computational plasticity—fundamentals and applications. Proceedings of the fifth international conference on computational plasticity. Barcelona, Spain: CIMNE; 1997. p. 239–54.
- [44] de Borst R, Schipperen JHA. Computational methods for delamination and fracture in composites. In: Allix O, Hild F, editors. Continuum damage mechanics of materials and structures. Elsevier Science Ltd.; 2002. p. 325–52.
- [45] Shet C, Chandra N. Analysis of energy balance when using cohesive zone model to simulate fracture processes. J Eng Mater Technol 2002;124:440–50.
- [46] Zou Z, Reid SR, Li S. A continuum damage model for delaminations in laminated composites. J Mech Phys Solids 2003;51(2):333–56. doi:10.1016/S0022-5096(02)00075-3.
- [47] de Andrés A, Pérez JL, Ortiz M. Elastoplastic finite element analysis of three-dimensional fatigue crack growth in aluminum shafts subjected to axial loading. Int J Solids Struct 1999;36(15):2231–58. doi:10.1016/S0020-7683(98)00059-6.
- [48] Ortiz M, Pandolfi A. Finite-deformation irreversible cohesive elements for three-dimensional crack-propagation analysis. Int J Numer Methods Eng 1999;44(9):1267–82. doi:10.1002/(SICI)1097-0207. (19990330)44:9<1267::AID-NME4863.0.CO;2-7.
- [49] Balzani C, Wagner W. Delamination analysis of UD composites using interface elements. Proc Appl Math Mech 2006;6:151–2. doi:10.1002/pamm.200610056.
- [50] Balzani C, Wagner W. An interface element for the simulation of delamination in unidirectional fiber-reinforced composite laminates. Eng Fract Mech 2008;75:2597–615. doi:10.1016/j.engfracmech.2007.03.013.
- [51] Wagner W, Balzani C. Simulation of delamination in stringer stiffened fiber-reinforced composite shells. Comput Struct 2008;86(9):930–9. doi:10.1016/j.compstruc.2007.04.018.
- [52] Rose JH, Ferrante J, Smith JR. Universal binding energy curves for metals and bimetallic interfaces. Phys Rev Lett 1981;47(9):675–8.

- [53] Camanho PP, Dávila CG. Mixed-mode decohesion finite elements for the simulation of delamination in composite materials. Technical memorandum TM-2002-211737. Hampton, VI 23681-2199, USA: NASA, Langley Research Center; 2002.
- [54] Camanho PP, Dávila CG, de Moura MF. Numerical simulation of mixed-mode progressive delamination in composite materials. *J Compos Mater* 2003;37(16):1415–38, doi:10.1177/002199803034505.
- [55] Korjakins A, Ozolinsh O, Rikards R. Investigation of degradation by tests and development of degradation models—contribution to deliverable D07 (data base of degradation models), COCOMAT technical report. Riga, Latvia: Riga Technical University; 2005.
- [56] Büsing S, Reimerdes H-G. Additional fracture toughness and pull-off tests. COCOMAT technical report. Work package 2, task 2.2. Aachen, Germany: RWTH Aachen University; 2008.
- [57] COCOMAT—specific targeted research project co-funded by the European Commission, priority aeronautics and space, 6th framework program, contract no. AST3-CT-2003-502723. <<http://www.cocomat.de>>.
- [58] Degenhardt R, Rolfes R, Zimmermann R, Rohwer K. COCOMAT—Improved Material exploitation of Composite airframe structures by accurate simulation of postbuckling and Collapse. *Compos Struct* 2006;73(2):175–8, doi:10.1016/j.compstruct.2005.11.042.
- [59] ASTM Standard D2344/D2344M-00(2006). Standard test method for short-beam strength of polymer matrix composite materials and their laminates. West Conshohocken, PA, USA: American Society for Testing and Materials; 2006.
- [60] Benzaggagh ML, Kenane M. Measurement of mixed-mode delamination fracture toughness of unidirectional glass/epoxy composites with mixed-mode bending apparatus. *Compos Sci Technol* 1996;56(4):439–49, doi:10.1016/0266-3538(96)00005-X.
- [61] Villaverde BN. Variable mixed-mode delamination in composite laminates under fatigue conditions: testing and analysis. PhD thesis. Girona, Spain: University of Girona, Department of Physics; 2004.
- [62] Whitcomb JD. Analysis of instability-related growth of a through-width delamination. Technical memorandum TM-1984-86301. Hampton, VI 23665-5225, USA: NASA, Langley Research Center; 1984.
- [63] Donaldson SL. The effect of interlaminar fracture properties on the delamination buckling of composite laminates. *Compos Sci Technol* 1987;28(1):33–44, doi:10.1016/0266-3538(87)90060-1.
- [64] Hashemi S, Kinloch AJ, Williams JG. Mechanics and mechanisms of delamination in a poly fiber composite. *Compos Sci Technol* 1990;37(4):429–62, doi:10.1016/0266-3538(90)90013-U.
- [65] Yan XQ, Du SY, Wang D. An engineering method of determining the delamination fracture toughness of composite laminates. *Eng Fract Mech* 1991;39(4):623–7, doi:10.1016/0013-7944(91)90212-J.
- [66] Greenhalgh E, Asp L, Singh S. Delamination resistance, failure criteria and fracture morphology of 0°/0°, 0°/5° and 0°/90° ply interfaces in CFRP. In: Fifth international conference on deformation and fracture of composites. London, United Kingdom; 1999.
- [67] Donaldson SL. Fracture-toughness testing of graphite epoxy and graphite peek composites. *Composites* 1985;16(2):103–11.
- [68] Hahn HT. A correlation between fracture energy and fracture morphology in mixed-mode fracture of composites. In: Fourth international conference on the mechanical behaviour of materials. Stockholm, Sweden; 1983. p. 431–8.
- [69] Hahn HT. A mixed-mode fracture criterion for composite materials. *Compos Technol Rev* 1983;5:26–9.
- [70] White SR. Mixed-mode interlaminar fracture of graphite/epoxy composites. Master's thesis. St. Louis, MI, USA: Washington University; May 1987.
- [71] Gnuplot—a portable command-line driven graphing utility, release 4.4.0; 2010 <<http://www.gnuplot.info>>.
- [72] Donaldson SL. Mode III interlaminar fracture characterization of composite materials. *Compos Sci Technol* 1988;32(3):225–49, doi:10.1016/0266-3538(88)90022-X.
- [73] Martin RH. Evaluation of the split cantilever beam for mode III delamination testing. Technical memorandum NASA-TM-101562. Hampton, VI 23665-5225, USA: NASA, Langley Research Center; 1989.
- [74] Lee SM. An edge crack torsion method for mode III delamination fracture testing. *J Compos Technol Res* 1993;15(3):193–201, doi:10.1520/CTR10369J.
- [75] Li J. Three-dimensional effect in the prediction of flange delamination in composite skin-stringer pull-off specimens. *J Compos Technol Res* 2002;24(3):182–9, doi:10.1520/CTR10568J.